AIP | Journal of Applied Physics

Size- and structure-dependence of thermal and mechanical behaviors of single-crystalline and polytypic superlattice ZnS nanowires

Junghwan Moon, Maenghyo Cho, and Min Zhou

Citation: Journal of Applied Physics **117**, 214307 (2015); doi: 10.1063/1.4921974
View online: http://dx.doi.org/10.1063/1.4921974
View Table of Contents: http://scitation.aip.org/content/aip/journal/jap/117/21?ver=pdfcov
Published by the AIP Publishing

JOURNAL OF APPLIED PHYSICS **117**, 214307 (2015)

Size- and structure-dependence of thermal and mechanical behaviors of single-crystalline and polytypic superlattice ZnS nanowires

Junghwan Moon,[1] Maenghyo Cho,[1] and Min Zhou[2,a)]
[1]*School of Mechanical and Aerospace Engineering, Seoul National University, Seoul 151-742, South Korea*
[2]*The George W. Woodruff School of Mechanical Engineering, School of Materials, Science and Engineering, Georgia Institute of Technology, Atlanta, Georgia 30332-0405, USA*

(Received 3 February 2015; accepted 21 May 2015; published online 2 June 2015)

Molecular dynamics (MD) simulations are carried out to study the thermal and mechanical behaviors of single-crystalline wurtzite (WZ), zinc-blende (ZB), and polytypic superlattice ZnS nanowires containing alternating WZ and ZB regions with thicknesses between 1.85 nm and 29.62 nm under tensile loading. The wires analyzed have diameters between 1.77 nm and 5.05 nm. The Green-Kubo method is used to calculate the thermal conductivity of the wires at different deformed states. A non-equilibrium MD approach is used to analyze the thermal transport behavior at the interfaces between different structural regions in the superlattice nanowires (SLNWs). The Young's modulus and thermal conductivity of ZB nanowires are approximately 2%–12% and 23%–35% lower than those of WZ nanowires, respectively. The lower initial residual compressive stress due to higher irregularity of surface atoms causes the Young's modulus of ZB nanowires to be lower. The dependence of the thermal conductivity on structure comes from differences in phonon group velocities associated with the different wires. The thermal conductivity of polytypic superlattice nanowires is up to 55% lower than that of single-crystalline nanowires, primarily because of phonon scattering at the interfaces and the resulting lower effective phonon mean free paths for each structural region. As the periodic lengths (1.85–29.62 nm) and specimen lengths (14.81–59.24 nm) of SLNWs decrease, these effects become more pronounced, causing the thermal conductivity to further decrease by up to 30%. *© 2015 AIP Publishing LLC*.
[http://dx.doi.org/10.1063/1.4921974]

I. INTRODUCTION

Nanowires are attractive 1-D structures because of their novel properties compared with bulk materials. These properties are attributed to high surface-to-volume ratios. Semiconducting nanowires are used in photonic, optoelectronic, piezoelectric, and thermoelectric devices.[1–5] Zinc sulfide (ZnS) is one of the II–VI inorganic semiconductor groups and has a variety of potential applications in LEDs, sensors, and UV lasers,[6–8] because of its wide band gap energy (3.72 eV for bulk wurtzite (WZ) and 3.77 eV for bulk zinc-blende (ZB))[9] and relatively good transport properties. Many researchers have synthesized various ZnS nanostructures such as nanowhiskers, nanowires, nanobelts, nanorods, and nanosheets.[10–16] Zinc sulfide is commonly found in either the cubic ZB form at ambient conditions or in the hexagonal WZ at high temperatures. The local atomistic structures of both polytypes are similar but different in the stacking sequences of Zn-S layers.[17] WZ ZnS nanowires usually grow along [100], [210], $[1\bar{1}0]$ directions on CdS nanoribbon[18] and [0001] direction on ZnS nanoribbon.[19] ZB ZnS nanowires usually grow along the [111] direction on SiO_2/Si substrates.[20] In general, WZ nanowires grow along the [0001] direction and ZB nanowires grow along the [111] direction. Furthermore, with the advances in nano-scale engineering techniques, nanowires can be easily fabricated to be heterogeneous structures. In the case of III-V semiconducting nanowires, Gudiksen *et al.*[21] synthesized GaAs/GaP superlattice nanowires by repeated modulation of the semiconductor reactants during growth of nanowires. Also, InP/InAs and InAs/GaAs heterogeneous superlattice nanowires (SLNWs) have been synthesized.[22,23] In addition to the heterogeneous SLNWs, homogeneous SLNWs with just lattice structure modulation, called polytypic SLNWs, have been manufactured.[24–26] Experimental observations and theoretical calculations[24,27–30] have proved that the growth diameter, temperature, and III/V ratio determine the WZ fraction of polytypic SLNWs. Engineering technologies to control precisely diameter-independent polytypic SLNWs are developing rapidly. For the II-VI groups, ZnS has the potential to yield various nanostructures. The ZnS/ZnO core-shell nanowires have been synthesized[31] and vertically aligned ZnS/ZnO nanowires[32] can be used for energy generation. The ZnS/ZnO biaxial nanobelts show unique cathodoluminescence properties and wide-range photoresponse.[33,34] It is known that heterocrystalline ZnS (WZ)/ZnS (ZB) nanobelts in the length direction and transverse direction can also be synthesized.[33,35–37] Notably, polytypic SLNWs have potential applications in new optical devices, mini-band engineering because of the difference in the electronic band structures between WZ and ZB nanowires.[26,38]

Many researchers utilized molecular dynamics simulations to analyze the mechanical and thermal behaviors of nanowires. Kulkarni *et al.*[39] studied polymorphic transitions

---

[a)] Author to whom correspondence should be addressed. Electronic mail: min.zhou@gatech.edu. Tel.: 404-894-3294. Fax: 404-894-0186.

TABLE I. Characteristic dimensions of nanowires.

WZ [0001]			ZB [111]		
Length (nm)	Diameter (nm)	No. of atoms	Length (nm)	Diameter (nm)	No. of atoms
14.78	1.93	2592	14.99	1.77	1952
	3.47	8400		3.53	6944
	5.01	14112		5.05	12704

of WZ ZnO nanowires under loading. Jung *et al.*[40] confirmed the coupling between the thermal and mechanical behaviors of WZ GaN nanowires when strains are induced. The thermal conductivity of SLNWs has been calculated via non-equilibrium molecular dynamics (NEMD) simulations. Lin and Strachan[41] discussed the effect of periodic length on the thermal conductivity of Si/Ge SLNWs and superlattice thin films (SLTFs). Samvedi and Tomar[42] analyzed the role of straining and morphology in determining the thermal conductivity of a set of Si/Ge SLTFs and biomimetic Si/Ge nanocomposites. Termentzidis *et al.*[43] observed a decrease of thermal conductivity of SiC nanowires with lattice and diameter modulations.

In this paper, we carried out molecular dynamics simulations to effect tensile loading to single-crystalline WZ ZnS nanowires grown along the [0001] direction and ZB wires grown along the [111] direction. We calculated the variation of thermal conductivity when mechanical strain is induced in the wires. The calculations allow the dependence of the thermo-mechanical behaviors of these single-crystalline ZnS nanowires on their atomistic structures to be analyzed. Additionally, the thermal and mechanical behaviors of the polytypic superlattice ZnS nanowires are compared with those of the single-crystalline nanowires. In particular, we note that lower thermal conductivity of SLNWs is desired in thermoelectric applications in order to enhance the figure of merit (ZT).[44–47] Although many papers have dealt with the characteristics of thermal transport between two different materials such as Si/Ge SLNWs and SLTFs, there is a lack of studies on the thermal behavior of NWs with heterogeneous structures, especially for conditions involving mechanical strain. The results from this analysis are expected to help understanding the thermal transport between different crystalline structural regions in nanomaterials and quantify the thermal and mechanical responses of the NWs.

II. FRAMEWORK OF ANALYSIS

A. Modeling of nanowires

Wurtzite (2H) and Zinc-blende (3C) are the most common structures of the semiconductor compounds that obey the octet rule. The WZ nanowire considered in this study consists of repeated structure units of two Zn-S layers (ABABAB…) stacked along the [0001] direction, while the ZB nanowire has three Zn-S layers (ABCABC…) stacked along the [111] direction.[17,48,49] First, single-crystalline nanowires with the WZ structure and the ZB structure are constructed. Both nanowires have hexagonal cross sections. The WZ nanowire is oriented in the [0001] direction and has $\{01\bar{1}0\}$ lateral surfaces. Likewise, the axis of ZB nanowire is along the [111] direction and the cross sections have six facets. Periodic boundary conditions are assigned along the axial direction. In order to compare the behaviors of wires of each structure, the characteristic dimensions (length and diameter) of the WZ and ZB nanowires are varied. The dimensions of the nanowires considered are shown in Table I. Figures 1(a) and 1(b) show the configurations of the WZ and ZB single-crystalline nanowires. Following the construction of the single crystalline wires, the polytypic SLNW is generated. The configuration involves repeated structure units of ZnS (WZ [0001])/ZnS (ZB [111]) along the axial direction. The periodic lengths of the blocks are same. In order to make periods the same, 3(2H) (ABABAB) and 2(3C) (ABCABC) segments are chosen to be the smallest unit segments. Figure 1(c) shows how the blocks in the superlattice ZnS nanowire are built. Five different periodic lengths (1.85, 3.70, 7.41, 14.81, 29.62 nm)

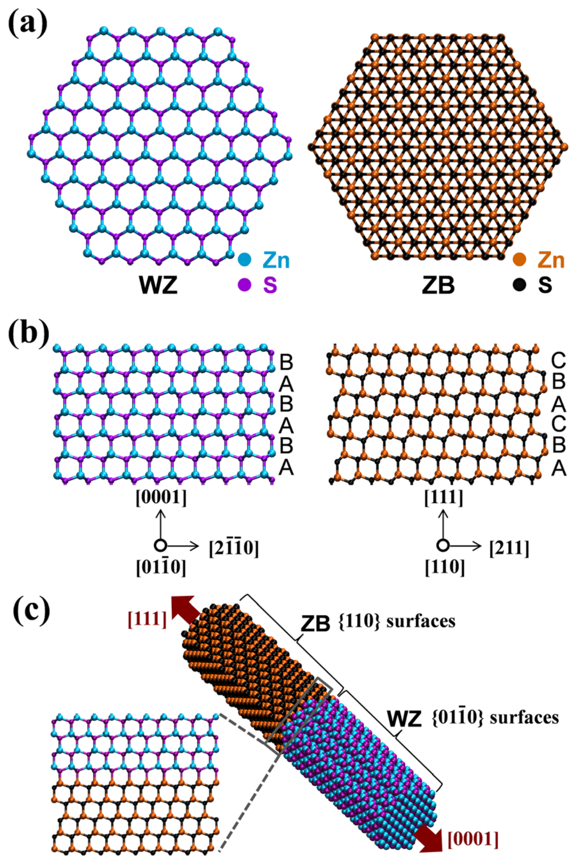

FIG. 1. (a) Configurations of cross sections, (b) stacking sequences of wurtzite, zinc-blende ZnS nanowires, and (c) MD model of polytypic superlattice ZnS nanowires.

and three specimen lengths (14.81, 29.62, 59.24 nm) are considered. Lattice mismatch exists between the two different structures. To accommodate the mismatch, initial transverse and axial distances between atoms in each unit cell are averaged for both structures. This approach has been used for other heterogeneous nanostructures.[41,50,51] The modified lattice constant is 5.43 Å for ZB and a = 3.84 Å and c = 6.27 Å for WZ.

B. Molecular dynamics simulations

All molecular dynamics (MD) simulations are conducted using the LAMMPS code developed by the Sandia national laboratory.[52] Temperature is controlled by the Nosé-Hoover algorithm.[53] Short-range interatomic forces are described by the Buckingham potential of Wright and Jackson[54] and long-range coulombic forces are calculated by the wolf summation method.[55] Buckingham-type pair potentials predict the phase transformation from WZ to BCT well under tensile loading.[39,40,56,57]

Before loading is applied, the nanowires are equilibrated for 100 ps using the NPT ensemble. After equilibration, tensile loading is applied by using an approximate quasi-static deformation scheme. Specifically, 0.2% strain increments are induced at a nominal strain rate of 0.05 ns^{-1} at each loading step. It is known that high strain rate changes the deformation of nanowire from a crystalline to an amorphous construction.[58,59] In addition, this structural transition can modify the behavior of nanowires.[60] The strain rate considered here is sufficiently low to predict the mechanical behaviors of nanowires precisely. At each increment, relaxation of the structure is carried via equilibration using the NVT ensemble for 40 ps at 300 K. Subsequently, the Green-Kubo method[61] is used to evaluate the thermal conductivity at each strain increment. This is an equilibrium molecular dynamics (EMD) approach for calculating the thermal conductivity. The heat flux in the length direction is calculated during the NVE ensemble for 2 ns via

$$J = \sum_{i=1}^{N}\left(v_i E_i + \frac{1}{2}\sum_{j=1, j\neq i}^{N} r_{ij}(F_{ij}\cdot v_i)\right). \tag{1}$$

Here, J is the heat flux, N is the number of atoms in the system, and E_i and v_i are the energy and velocity of the atom i, respectively. r_{ij} is the distance between atoms i and j, and F_{ij} is the force between i and j. The first term ($v_i E_i$) is neglected because it is related to the heat convection, not conduction. The thermal conductivity at each strain state is calculated via

$$\kappa(\tau_m) = \frac{1}{V k_B T^2}\int_{\tau_0}^{\tau_m} \langle J(t) J(\tau_0)\rangle dt, \tag{2}$$

where κ is the thermal conductivity, τ_m is the delay time, k_B is the Boltzmann constant, V is volume, T is temperature, and $\langle J(t)J(\tau_0)\rangle$ is the auto-correlation function of heat flux. The truncation delay time is 2–5 ps because longer delay times cause statistical error. Results from at least five MD simulations with different initial atomic velocities are averaged to calculate the thermal conductivity. Because the Debye temperature is relatively low (340–380 K (Refs. 62 and 63) for both WZ and ZB ZnS), quantum correction of thermal conductivity is neglected at T = 300 K.

To confirm the results of the EMD approach and investigate the effect of interfaces on the thermal behaviors of the polytypic SLNWs, a reverse-NEMD approach proposed by Müller-Plathe[64] is also used. Figure 2 shows the configuration of the system used in this approach. The system is divided into N bins along the axial direction. Bin 1 and bin N are the heat sink locations and bin N/2 + 1 is the heat source location. The heat flux is imposed by exchanging velocities between the hottest atom in the heat sinks and the coldest atom in heat source. Some analyses of amorphous/crystalline silicon superlattices use the thermostats consisting of half amorphous and half crystalline phases.[65–67] However, the phases of heat sink and heat source only change the thermal conductivity by approximately 0.36% in one of our NEMD models. Therefore, the effect of phases of thermostats is not considered here. Because the systems considered in the reverse-NEMD approach consist of more atoms than those considered in the EMD approach, longer times are needed for initial relaxation. As a result, the systems are equilibrated for 50 ps using the NPT ensemble at 300 K and then for 100 ps using the NVT ensemble at 300 K. After the initial relaxation, the velocities of the atoms are exchanged for 5 ns to apply the heat flux and create a temperature gradient. To prevent excessive temperature rise and drop in the heat source and sinks, the NVT ensemble at 300 K is carried out during the exchange of velocities. These simulation steps are carried out for the nanowire with the diameter of 3.51 nm and length of 14.81 nm. When either the diameter or length increases, the relaxation times are chosen to be proportional to the sizes. The heat flux and temperature gradient converge at 1 ns. So, the averaged heat flux and temperature gradient between 1 and 5 ns are used to calculate the thermal conductivity via

$$\kappa = \frac{J}{|\nabla T|}, \tag{3}$$

where κ is the thermal conductivity, J is the heat flux, and ∇T is the temperature gradient. Heat fluxes generated range from $6.64 \times 10^9\ \text{W/m}^2$ to $1.05 \times 10^{10}\ \text{W/m}^2$. The temperature differences between the heat source and sink are in the range of 50–90 K. These ranges of heat flux and temperature gradient satisfy the Fourier's linearity requirement compared with those of other NEMD simulations.[68,69] The thermal resistivity W at the interface and for the whole specimen can also be obtained via

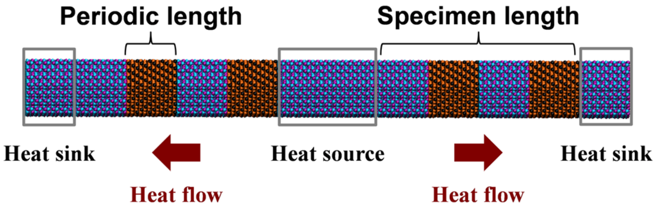

FIG. 2. NEMD model of polytypic superlattice ZnS nanowires.

$$W = \frac{1}{\kappa} = \frac{|\nabla T|}{J}. \tag{4}$$

III. RESULTS AND DISCUSSION

A. Single-crystalline ZnS nanowires

First, the mechanical and thermal behaviors of the WZ and ZB single-crystalline nanowires are analyzed. Figure 3 shows the stress-strain curves of WZ and ZB nanowires whose diameters range from 1.93 to 5.01 nm and 1.77 to 5.05 nm, respectively. The virial formula modified by Zhou[70] is used to calculate the stress. When tensile loading is applied, the WZ nanowire with the [0001] orientation shows an elastic behavior as the strain increases from 0 to approximately 0.1. Subsequently, the stress drops precipitously. The drop is associated with the change of the WZ structure to the body-centered-tetragonal (BCT) structure. The core part of the WZ nanowire is transformed into the BCT structure, and consequently, the surface layer is rearranged. Accordingly, the atomistic structures of the core and the surface regions become different after the transition. This phase transformation has been reported for other WZ nanowires, such as ZnO and GaN.[39,40] BCT ZnS nanocrystals have been synthesized via chemical coprecipitation.[71] Phase transition from WZ to BCT for ZnS has also been predicted by theoretical calculations.[72,73] After the initiation of the phase transformation, the stress gradually increases as the phase transformation propagates throughout the wire. After the whole wire is in the BCT state, the final event of loading is a sharp stress drop at a strain between 0.17 and 0.19 associated with the BCT-structured nanowire separating into two parts. Figure 3(a) shows that the diameter of the WZ nanowires affects their mechanical behaviors. The Young's modulus and critical stress for phase transformation increase up to 20.1% and 23.5%, respectively, as the diameter decreases from 5.01 nm to 1.93 nm. This trend also appears in the elastic behaviors of the BCT-structured wires. The variations of Young's modulus (50.2%) and critical peak stress (41.1%) in the BCT-structured wires are higher than those of the initial WZ-structured wires. When the diameter of the WZ nanowires increases to approximately 5 nm, the young's modulus approaches that of bulk WZ. This size effect appears because the surface-to-volume ratio increases as the size of nanowire decreases.

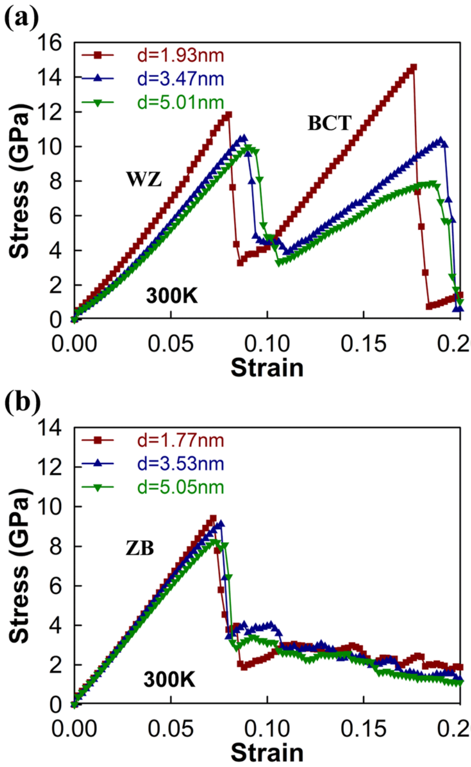

FIG. 3. Stress-strain curves of single-crystalline (a) WZ and (b) ZB ZnS nanowires at T = 300 K.

Figure 3(b) shows that the size effect is also observed for the ZB nanowires. Table II compares the mechanical properties of WZ, BCT, and ZB nanowires of similar sizes. The Young's modulus and critical stress of ZB nanowires are up to 11.6% and 9.8% lower than those of WZ nanowires, respectively. This difference is due to the different surface structures of the nanowires. Figure 4 shows the distributions of stress in the axial direction for the WZ, ZB, and BCT nanowires. The residual compressive stress on the surface of the WZ nanowire is the highest. It has been shown that the residual stress on the surface significantly influences the stiffness of nanowires.[74] The different stacking sequences in the axial direction between the three structures contribute to the different configurations of surfaces and, hence, the different residual stress levels and Young's modulus values. The structural difference also leads to different failure characteristics. Figure 5 shows the configurations of the two nanowires after fracture. While the brittle fracture occurs in the transformed BCT structures at a strain between 0.17 and 0.19, the ZB nanowire does not show the phase transformation and the stress abruptly drops at a strain about 0.08 due to bond breakage. Before the stress drops, there is no

TABLE II. Young's modulus and critical stress of (a) WZ, (b) BCT, and (c) ZB nanowires.

	Young's modulus (GPa)	Critical stress (GPa)
(a) Diameter (nm)	WZ	
1.93	150.25	11.85
3.47	129.57	9.61
5.01	120.01	9.06
Bulk	118,[85] 128[86]	
(b) Diameter (nm)	BCT	
1.93	137.19	14.95
3.47	80.03	11.97
5.01	68.26	8.8
Bulk		
(c) Diameter (nm)	ZB	
1.77	132.82	10.68
3.53	120.92	9.14
5.05	117.49	8.93
Bulk	107.7[87]	

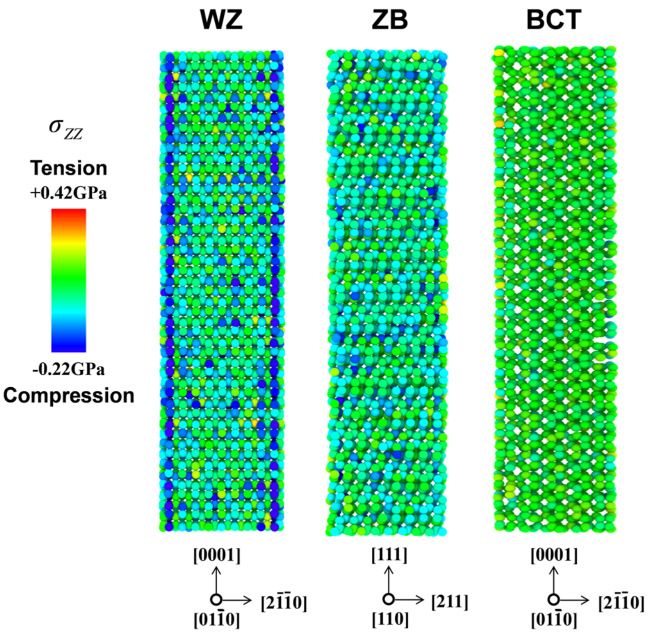

FIG. 4. Stress distributions on the $(01\bar{1}0)$ cross section of WZ (left), (110) cross section of ZB (center), and $(01\bar{1}0)$ cross section of BCT (right) nanowires.

structural defect or plastic deformation. Bond breakage is observed initially on the outmost surface and progresses via cleavage. Fracture planes show reorientation along inclined bands. ZB CdSe nanowires show similar brittle fracture.[75]

Figure 6 shows the thermal conductivity of WZ and ZB nanowires as a function of strain calculated using the Green-Kubo method. The thermal conductivity of the WZ nanowires decreases 26.9%–38.9% as the strain increases to the point for the onset of phase transformation. Also, as the strain approaches the critical point of fracture, the thermal conductivity of the ZB nanowires decreases 29.1%–40.8%. This phenomenon arises from the dependence of phonon relaxation time on strain.[76] In crystalline structures of the nanowires, heat is transported mainly by phonons and the thermal conductivity is related to the phonon relaxation time. Under tensile loading, phonon relaxation time and thermal conductivity decrease. Indeed, the size effect also appears in the thermal conductivity of both single-crystalline nanowires. As the diameter decreases, the thermal conductivity for the two types of wires decreases by up to 33.2% and 40.2%, respectively. The thermal conductivity of bulk ZB ZnS is approximately 27 W/(mk).[77,78] The decrease of thermal conductivity of ZnS nanowires relative to that of bulk is due to phonon scattering at the wire surfaces. As the diameter decreases, the proportion of surface atoms increases and the effect of surface phonon scattering intensifies. As a result, the thermal conductivity decreases.

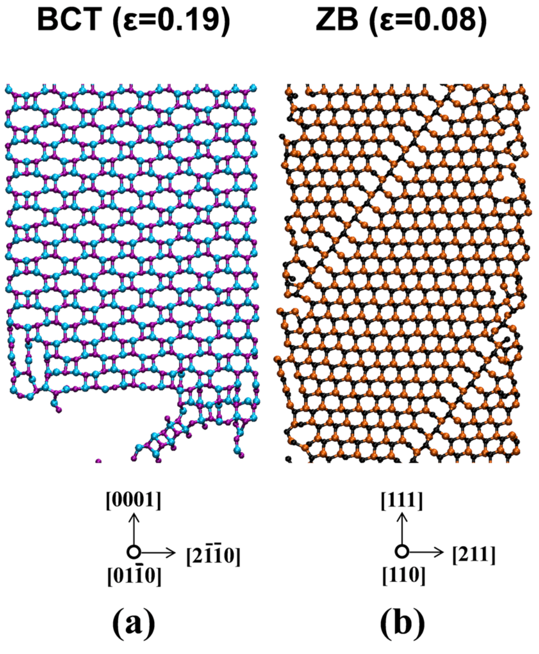

FIG. 5. Atomic configurations when the fracture occurs on (a) $(01\bar{1}0)$ cross section of WZ nanowire and (b) (110) cross section of ZB nanowire.

Figure 6 reveals that the thermal conductivity of the transformed wires in the BCT structure (strain = 0.1–0.2) is 30.2%–49.9% lower than that of WZ structured wires (strain = 0–0.1). Also, the thermal conductivity of ZB nanowires is 23.3%–35.1% lower than that of WZ wires and 14.9%–25.4% higher than that of BCT wires. This trend of thermal conductivity is in agreement with that for Young's modulus (Table II). According to the kinetic theory of heat transfer, the lattice thermal conductivity can be given as

$$\kappa = \frac{1}{3}Cvl = \frac{1}{3}Cv^2\tau, \tag{5}$$

κ is lattice thermal conductivity, C is specific heat, v is phonon group velocity, l is phonon mean free path, and τ is

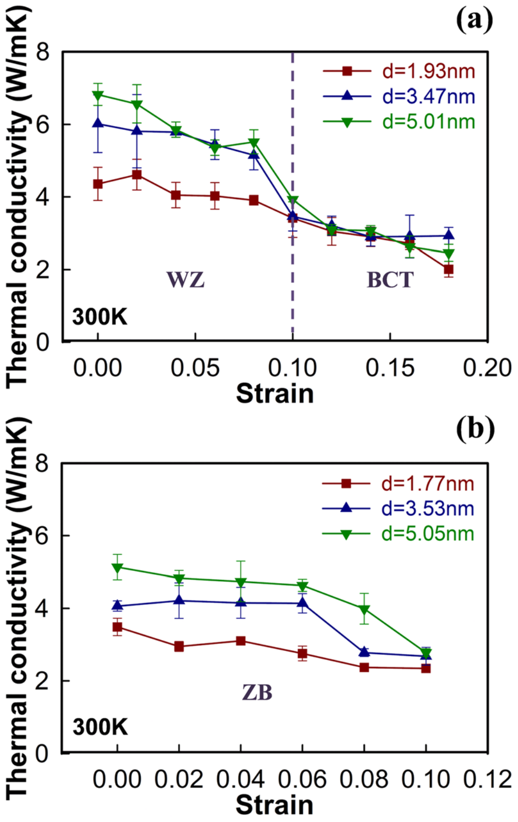

FIG. 6. Thermal conductivity as a function of strain of (a) WZ and (b) ZB ZnS nanowires at T = 300 K.

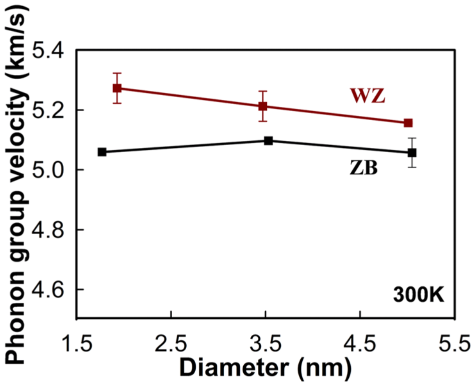

FIG. 7. Phonon group velocity as a function of the diameter of nanowires. T = 300 K.

phonon relaxation time. The lattice thermal conductivity is proportional to the phonon group velocity v, which is proportional to the elastic constant and can be approximated using a harmonic average of longitudinal and transverse wave velocities[79] as

$$v_L = \sqrt{\frac{C_{33}}{\rho}}, v_T = \sqrt{\frac{C_{44}}{\rho}}, \tag{6}$$

where v_L is longitudinal wave velocity, v_T is transverse wave velocity, ρ is mass density, and C_{33} and C_{44} are the elastic constants. The phonon group velocities of the WZ and ZB structures are shown in Fig. 7. The changes in group velocities with increasing diameter are very small for both structures. However, the structure dependence of thermal conductivity comes from the phonon group velocity. For similar ranges of diameter, the phonon group velocities of WZ nanowires are higher than those of ZB nanowires. This trend is consistent for mechanical and thermal behaviors.

B. Polytypic superlattice ZnS nanowires

Table III compares the mechanical properties of the single-crystalline nanowires and polytypic SLNWs. The Young's modulus of the SLNW with a diameter of 3.51 nm is 21.7%–27.0% lower than that of single-crystalline nanowires with essentially the same diameters. Additionally, the fracture stress of the SLNW is 24.4% lower than that of ZB wires and 28.1% lower than the stress at which the WZ structure transforms into the BCT structure. The difference in the Young's modulus between the single-crystalline wires and the SLNWs can be explained by their surface configuration and the interfaces. Figure 8 shows the distributions of the compressive stress in the length (z) direction and potential energies of the wires and bulk material after initial relaxation. The atoms of the WZ nanowire are well arranged in the region within a radius of 14.5–14.8 Å. Their potential energies are similar to those in the stable bulk state. These observations indicate reconstruction of only the surface which consists of two repeated Zn-S layers. The surface reconstruction occurs by the motions in opposite directions of the outermost layer and the second outermost layer. The surface of the ZB wire has lower compressive stresses. The surface of the SLNW has a combination of two different configurations. Because of the constraints from the ZB surfaces, the WZ segments do not have well-constructed surface layers. Furthermore, significant compressive stresses are applied on atoms in the interior. The difference between the interior and surface regions is less pronounced for the SLNW, contributing to lower stiffness values.

TABLE III. Comparison of Young's modulus and critical stress of single-crystalline and polytypic SLNWs. T = 300 K.

	WZ	ZB	SLNW
Diameter (nm)	3.47	3.53	3.51
Young's modulus (GPa)	129.57	120.92	94.65
Critical stress (GPa)	9.61	9.14	6.91

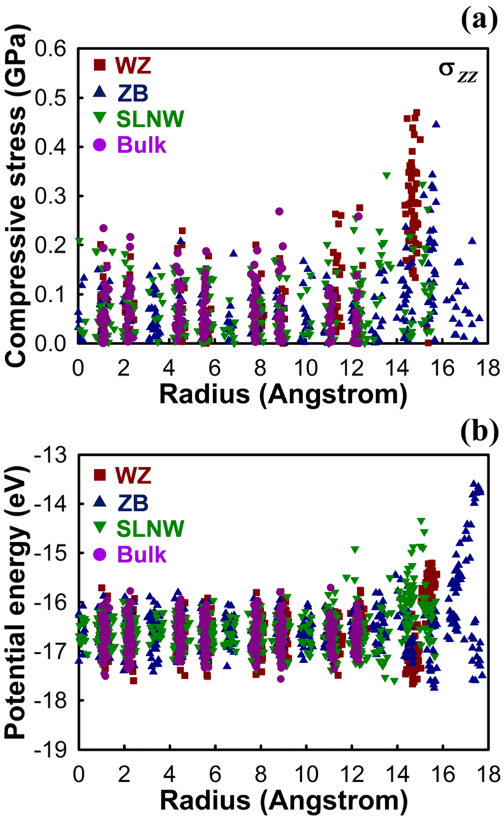

FIG. 8. Distributions of (a) compressive stress in the length direction (σ_{zz}) and (b) potential energies with respect to the position of atoms. T = 300 K.

Figure 9(a) shows the stress-strain curves of polytypic SLNWs whose diameter is 3.51 nm and length is 14.81 nm. The length of the periodic blocks, the periodic length (PL), is varied to investigate how it affects the behaviors of the SLNWs. The specimen length (SL) is chosen to be similar to that of the single-crystalline nanowires for comparison. Figure 9 shows that the periodic length (PL) only has a minor effect on the mechanical properties of the SLNWs. Figures 9(b) and 9(c) show the stress-strain curves of SLNWs with different specimen lengths. The results are similar. Failure of the SLNWs occurs when the tensile strain reaches approximately 0.07. The WZ-to-BCT transformation occurs just before wire failure and significantly affects the mechanism of fracture. No phase transformation is seen in the ZB structured regions. As a result, the coexistence of the BCT and

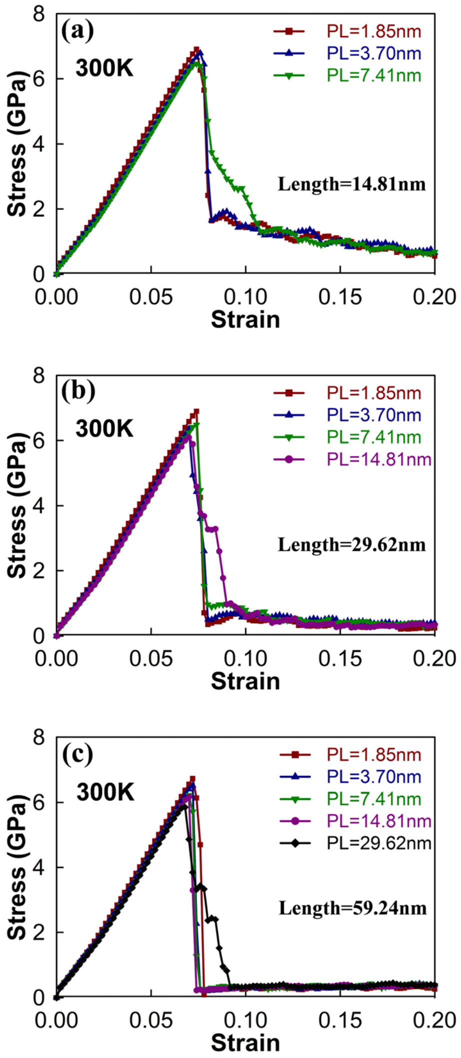

FIG. 9. Stress-strain curves of polytypic superlattice nanowires with different periodic lengths. Diameter d = 3.51 nm. Specimen length is (a) 14.81 nm, (b) 29.62 nm, and (c) 59.24 nm. T = 300 K.

ZB regions makes the structure of interfaces unstable, leading to large deformations and voids, followed by eventual fracture at the interfaces. Figure 10 shows the atomistic configuration of superlattice nanowire at an interface when fracture occurs.

The thermal conductivity of polytypic superlattice ZnS nanowires is analyzed. Figures 11(a)–11(c) show the thermal conductivity of the SLNWs as a function of strain. The results are obtained by the Green-Kubo method. Like the single-crystalline nanowires, the polytypic SLNWs show size dependence of thermal conductivity, which decreases 38.6%–44.9% as the diameter of nanowires decreases from 5.03 nm to 1.85 nm. As the tensile strain increases, the thermal conductivity decreases up to 43.1%. The reason is same as that for the single-crystalline nanowires. The thermal conductivity of the WZ nanowire whose diameter is 3.47 nm is approximately 6.02 ± 0.81 W/(mK). The thermal conductivity of the ZB nanowire with a diameter of 3.53 nm is approximately 4.05 ± 0.15 W/(mK). On the other hand, the thermal conductivity of the SLNW whose diameter is 3.51 nm and periodic length is 7.41 nm is approximately 3.15 ± 0.28 W/(mK). Clearly, the thermal conductivity of the SLNWs is

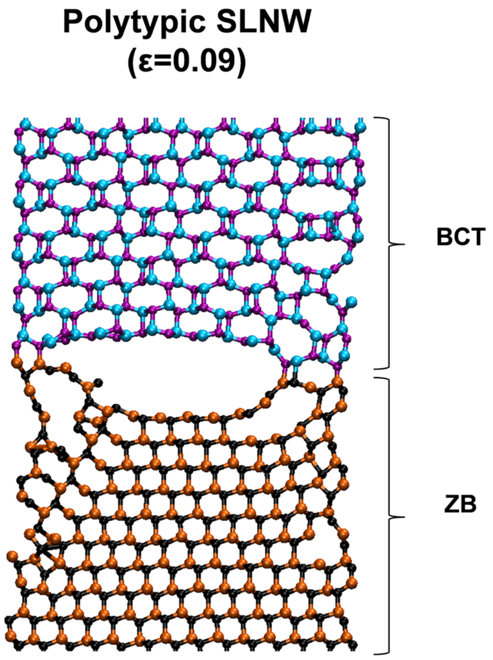

FIG. 10. Atomistic configuration of polytypic SLNW when fracture occurs. d = 3.51 nm, specimen length = 14.81 nm, T = 300 K.

lower than those of pristine WZ and ZB nanowires, owing to the interfaces between the two different structures. This is due to the acoustic impedance mismatch between the two structures. Although modified lattice constants are used to avoid lattice mismatch at the beginning of the simulations, the positions of atoms rearrange after relaxation to yield slightly different spacing between atomic layers of the two structures. Termentzidis *et al.*[43] also observed a reduction in thermal conductivity due to lattice and diameter modulation in SiC nanowires. The tendency in the thermal conductivity is consistent with that in the mechanical behaviors. It is useful to note that the thermal conductivity is even lower for wires with lower periodic length values and therefore higher numbers of interfaces, as seen in Fig. 11(d). The result is obtained using the reverse-NEMD approach and is similar to, but slightly lower than, the result from the Green-Kubo approach. The lower reverse-NEMD data is due to the fact that phonon scattering occurs at the heat sources and sinks. As mentioned before, since the periodic length does not significantly affect the stiffness and phonon group velocity of the SLNWs, other mechanisms are responsible for the lower thermal conductivity. One is phonon confinement due to the decrease in the periodic length and another is the phonon scattering at the interfaces.

The first reason should be considered when the length of the segments is on the same order as the phonon mean free path. The effective phonon mean free path is affected by the characteristic distance of phonon scattering. The relation can be approximated as[68]

$$\frac{1}{\kappa} = \frac{3}{Cv}\frac{1}{l_{eff}} = \frac{3}{Cv}\left(\frac{1}{l_{\infty}} + \sum \frac{1}{l_{scatter}}\right), \tag{7}$$

where l_{eff} is the effective mean free path, l_{∞} is the phonon mean free path for an infinite system, and $l_{scatter}$ is the specific

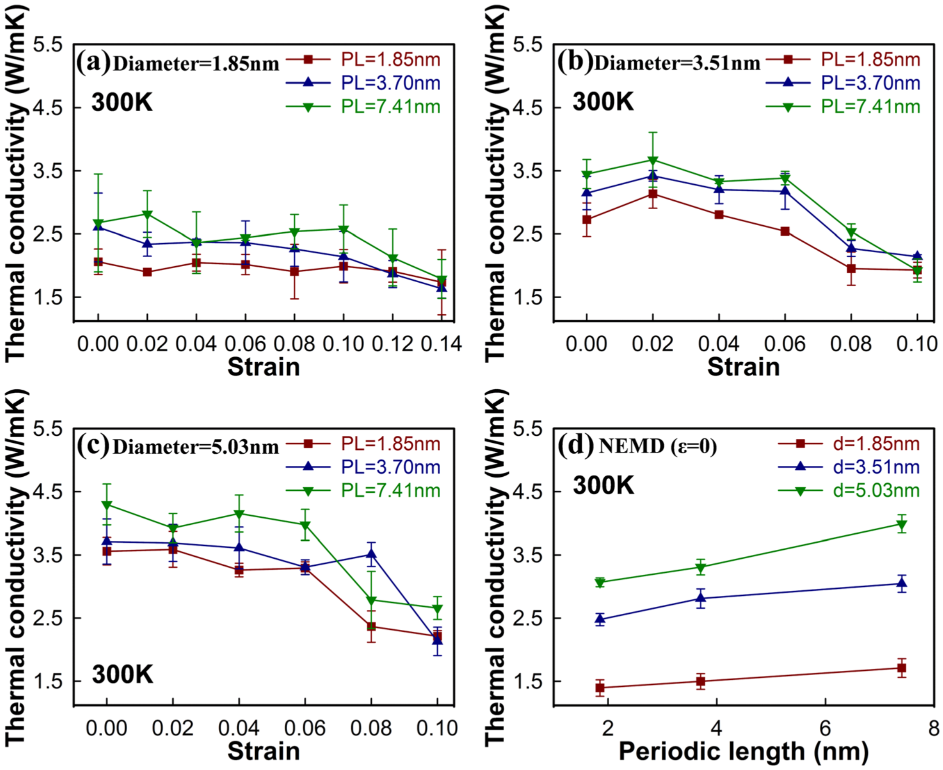

FIG. 11. (a)–(c) Thermal conductivity of SLNWs as a function of strain and periodic length. Length of nanowire: 14.81 nm (calculated by EMD approach. (a) diameter = 1.85 nm, (b) diameter = 3.51 nm, (c) diameter = 5.03 nm). (d) Thermal conductivity of SLNWs as a function of diameter and periodic length (calculated by NEMD approach).

distance between two phonon scattering events. This relation implies that the effective phonon mean free path and thermal conductivity can decrease as the distance between phonon constraints decreases. Figure 12 shows the relation between the inverse of thermal conductivity κ and the inverse of the length of each nanowire segment. For the single-crystalline nanowire segments, the constraints on the phonon waves exist at the heat source and sink. Therefore, $l_{scatter}$ can be regarded as the length of the nanowire (l_z). The linear fits to the MD data in Fig. 12 provide the thermal resistivity of each nanowire block in the SLNWs. When the data points for the long samples ($l_z = 18.52$–37.48 nm) are used for the linear fitting, the effective mean free paths of the two polytypes are almost the same. This is consistent with the result for SiC nanowires.[43] Data for longer samples ($l_z = 50$–400 nm) are needed to more precisely calculate the l_∞. However, the model in Fig. 12 is used to predict the thermal resistivity of each nanowire block in the SLNWs, accounting for the size effect. Because the stated range of periodic length is about 1.85–29.62 nm, calculations with longer samples are neglected.

The second reason for the lower thermal conductivity of the polytypic SLNWs is that the filtering of phonon wave packets occurs at the interfaces because of the difference in the characteristics of lattice vibrations. Figure 13 shows the temperature profile for one of the NEMD systems. The WZ and ZB segments have different temperature gradients and a small temperature jump can be observed at the interface. Some researchers also report that there is an abrupt temperature variation at interfaces of superlattice structures in NEMD simulations.[42,80] This effect is caused by the thermal boundary resistance and contributes to lowering the thermal conductivity of the structures. The temperature difference at the interface between the two polytypes is very small compared with results for structures with different materials. This is reasonable because the polytypic SLNWs consist of

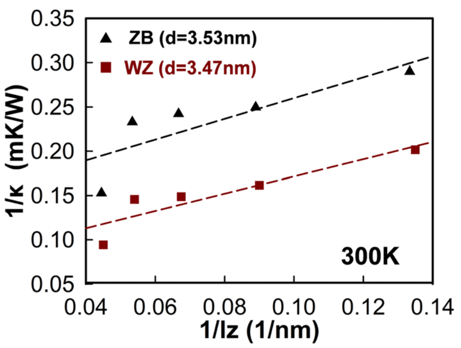

FIG. 12. Relations between the inverse of thermal conductivity and the inverse of the length of each nanowire structure region in NEMD simulations. T = 300 K.

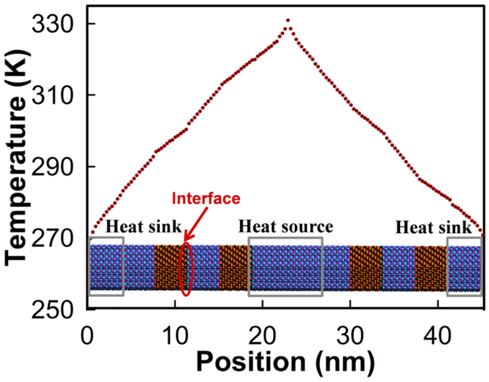

FIG. 13. Temperature profile for a polytypic ZnS SLNW. Periodic length = 3.70 nm, specimen length = 14.81 nm, d = 3.51 nm. The temperature gradients are used to calculate the thermal conductivity of the SLNWs.

the same material with different structures. The effect of interfaces on the thermal transport in SLNWs can be observed by comparing the phonon density of states (PDOS). The PDOS of the Zn-S layers of each structure at the interface are calculated using the Fourier transformation of velocity autocorrelation function (VACF) in the form of

$$\mathrm{VACF} = \langle v_i(0) \cdot v_i(t) \rangle. \tag{8}$$

The result is shown in Fig. 14. The data concerns the case of the periodic length of 7.41 nm and specimen length of 14.81 nm. The phonon wave-packets whose frequencies are, say, approximately 3, 6, and 10 THz partially pass through the interfaces when heat flows from WZ to ZB. Hence, some phonon waves are reflected and scattered and the effect intensifies as the number of interfaces increases.

The temperature profiles obtained by NEMD simulations are used to calculate the thermal conductivity of the SLNWs with different periodic lengths and specimen lengths. Based on the rule of mixture,[68] the thermal conductivity of the multi-layered structures can be expressed as

$$\kappa^{-1} = \sum_i f_i \kappa_i^{-1}, \tag{9}$$

where f_i is the volume fraction and κ_i is the thermal conductivity of each component. When this equation is applied to our NEMD model, the thermal conductivity of SLNWs can be calculated as

$$\begin{aligned} \frac{1}{\kappa} = W = -\frac{\Delta T}{LJ} &= -\frac{\sum\limits_{WZ} \Delta T_{WZ} + \sum\limits_{ZB} \Delta T_{ZB} + \sum\limits_{\mathrm{int}} \Delta T_{\mathrm{int}}}{LJ} \\ &= \sum_{WZ} W_{WZ} \frac{L_{WZ}}{L} + \sum_{ZB} W_{ZB} \frac{L_{ZB}}{L} + \sum_{\mathrm{int}} W_{\mathrm{int}} \frac{a_z}{L}, \end{aligned} \tag{10}$$

where W_{WZ} and W_{ZB} are the thermal resistivity of each structured segment. J is the heat flux and ΔT is the temperature variation from MD calculations. The temperature variations are calculated by linearly fitting the temperature profiles of the segments. L is the length of the whole specimen and L_{WZ} and L_{ZB} are the periodic lengths of each structural block. In particular, a_z is chosen as the lattice parameter in the heat transport direction to calculate the thermal resistivity of the interfaces (W_{int}). The overall resistivity is the sum of the products of thermal resistivity and volume fraction of structured segments and interfaces.

To predict the thermal conductivity of the SLNWs, we need to calculate the thermal resistivity of each structure and interfaces. First, the thermal conductivity of each nanowire block is predicted using Eq. (7) and linearly fitted graphs shown in Fig. 12. To consider the effects of the characteristic lengths on phonon scattering, $l_{scatter}$ is substituted with the periodic lengths and specimen lengths. The resistivity of the interfaces is predicted by calculating the thermal boundary resistance based on the acoustic mismatch model (AMM).[81] The thermal resistance of the interfaces is caused by differences in wave speeds of the materials. The AMM is suited for our model because the initial SLNWs have atomically sharp interfaces and lattice mismatch is very small. In this model, the transmission probability of phonons from material 1 to material 2 ($\alpha_{1\rightarrow 2}$) is estimated via[81]

$$\alpha_{1\rightarrow 2} = \frac{4Z_1 Z_2}{(Z_1 + Z_2)^2}, \quad Z_i = \rho_i v_i, \tag{11}$$

where Z_i is the acoustic impedance of materials, ρ_i is mass density, and v_i is the mean phonon speed. The transmission coefficient of the materials for mode of propagation j ($\Gamma_{1,j}$) is defined as[81]

$$\Gamma_{1,j} = \int_0^{\frac{\pi}{2}} \alpha_{1\rightarrow 2}(\theta, j) \cos\theta \sin\theta d\theta, \tag{12}$$

where θ is the angle between the incident direction of phonons and normal to an interface. To simplify the calculation, α is regarded as an independent function of the incident angle. The final form of thermal boundary resistance in the AMM ($R_{B,AMM}$) is expressed as[81]

$$R_{B,AMM} = \left[\frac{\pi^2}{15} \frac{k_B^4}{\hbar^3} \left(\sum_j v_{1,j}^{-2} \Gamma_{1,j} \right) \right]^{-1} T^{-3}, \tag{13}$$

where k_B is the Boltzmann constant, T is temperature, and $\hbar$ is Planck's constant divided by 2π. The thermal resistivity at the interface (W_{int}) is defined as the thermal boundary resistance ($R_{B,AMM}$) divided by the fictitious length of interface (a_z). Figure 15 compares the interface thermal resistivity

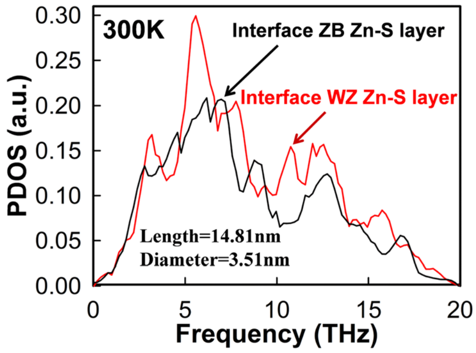

FIG. 14. Comparison of phonon density of states (PDOS) of WZ and ZB layers at the interface when heat flows from WZ to ZB. Periodic length = 7.41 nm, specimen length = 14.81 nm, d = 3.51 nm, T = 300 K.

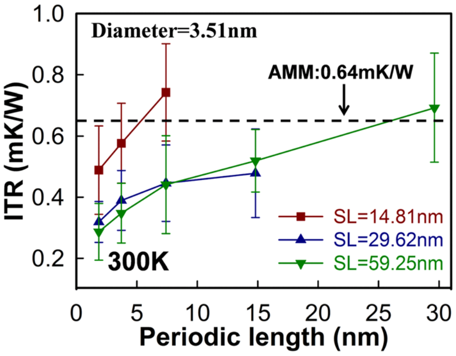

FIG. 15. Comparison of thermal resistivity at the interface obtained by MD simulations (solid lines) and the acoustic mismatch model (AMM). d = 3.51 nm, T = 300 K.

(ITR) obtained from the AMM calculation and MD temperature profiles. The diameter of the SLNW is 3.51 nm and both the periodic lengths (1.85–29.62 nm) and specimen lengths (14.81–59.24 nm) are varied to confirm their effects on the resistivity. The AMM result is very similar to the MD data. The difference of interface resistivity generated by heat flow direction is very small in both the AMM and MD models. That is, there is no drastic difference of thermal resistivity between heats flowing from WZ to ZB and from ZB to WZ. The reason is because the model considered here consists of the same materials and the acoustic impedance difference between the lattice structures is not large.

The thermal resistivity of the interfaces decreases as the periodic length decreases. This trend is also observed in other SLNWs in the NEMD simulations[41,82,83] and can be explained by using the cumulative phonon thermal conductivity with respect to the phonon wavelength.[41,84] Phonons whose wavelengths are shorter than the PL are dominantly scattered by the interfaces. With fixed overall specimen length, the fraction of energy transported by these phonons decreases as the periodic length decreases. The specimen length does not influence the interfacial thermal resistivity when it is over 29.62 nm. Only SLNWs with the length of 14.81 nm show high resistivity. This is because phonons whose wavelengths are over the SL cannot exist. When SL = 14.81 nm, phonons with medium wavelengths (10–30 nm) seen in wires with SL = 29.62 nm cannot exist. So, the fraction of scattered phonons at the interfaces and the ITR itself are higher than those of longer wires. However, the specimen length of real wires does not affect the ITR because their lengths are much longer than those in our simulations.

As expected, the thermal resistivity of interface regions is approximately 4–8 times higher than that of each nanowire segment. This value is much lower than what is reported in other studies involving interfaces between different solids. It is known that larger differences in the mass and bond strength between materials correspond to larger influence of interface on thermal transport.[80] However, for the same material with different structures, lower thermal resistivity at the interfaces is more reasonable. Using the thermal resistivity calculated via Eq. (7) and the AMM calculation, we predict the thermal conductivity of polytypic SLNWs shown in Fig. 16. There is a strong agreement between the prediction and MD calculations using the ratio of heat flux with temperature gradient. The predicted values are slightly lower than the results of NEMD simulations. This can be attributed to an overestimate of the effect of periodic length on effective phonon mean free path. The calculations obviously capture the changes of thermal conductivity with the periodic and specimen lengths of the SLNWs.

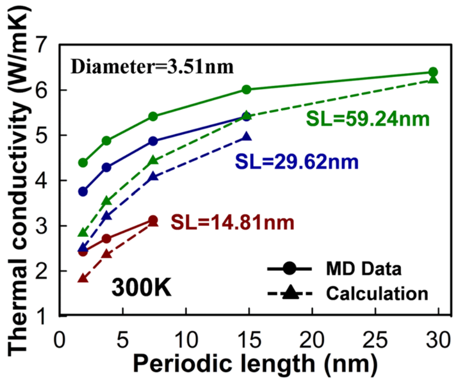

FIG. 16. Comparison of thermal conductivity of ZnS SLNWs obtained by MD simulation (solid lines) and model calculation (dashed lines). d = 3.51 nm, T = 300 K.

IV. CONCLUSIONS

The thermal and mechanical behaviors of ZnS single-crystalline and polytypic superlattice nanowires are investigated by atomistic simulations. The crystalline structure is a decisive factor affecting the thermo-mechanical behaviors of single-crystalline ZnS nanowires. When tensile loading is applied, [0001]-oriented WZ nanowires transform into the BCT structure while [111]-oriented ZB nanowires fail without any phase transformation. Distinct surface configurations of the structures give rise to different deformation behaviors. The lower residual compressive stress on the surfaces of ZB ZnS nanowires causes the Young's modulus to be 2%–12% lower than that of WZ ZnS nanowires. For composite ZnS nanowires with periodic WZ and ZB structural regions, fracture initiates from the interface during tensile deformation. The Young's modulus and thermal conductivity of ZnS SLNWs are up to 27% and 55% lower, respectively, compared with those of single-crystalline ZnS nanowires. Irregularity in the arrangement of surface atoms of the superlattice nanowires leads to lower initial compressive stress and Young's modulus.

The effects of the characteristic lengths on the thermo-mechanical behaviors of polytypic ZnS SLNWs are analyzed. The changes in the period and overall lengths do not significantly affect the mechanical behavior of the SLNWs. However, as the period and specimen lengths decrease, the thermal conductivity decreases by as much as 30%. This is because of a reduction in the effective phonon mean free path and an increase in the number of interfaces where phonon scattering occurs. The effects are quantified via calculations of the effective phonon mean free paths and thermal boundary resistance of interfaces using an acoustic mismatch model. The results of the simulations reported can be used to establish a relation between the microscopic crystal structure and corresponding thermo-mechanical properties of ZnS nanowires. The results are also useful in the understanding of thermal transport in complicated ZnS superlattice structures and in the design of ZnS SLNWs with desired properties. In particular, the mechanisms to take advantage of include the fact that polytypic SLNWs can achieve low thermal conductivity via smaller characteristic lengths, offering an alternative approach for enhancing thermoelectric performance of materials.

ACKNOWLEDGMENTS

Support by the National Research Foundation of Korea (NRF) grant funded by the Korea government (MSIP) (No. 2012R1A3A2048841) and Chinese Academy of Science through the CAS/SAFEA International Partnership Program for Creative Research Teams is gratefully acknowledged.

[1] W. Lu and C. M. Lieber, J. Phys. D: Appl. Phys. **39**, R387 (2006).
[2] W. Lu and C. M. Lieber, Nat. Mater. **6**, 841 (2007).
[3] A. I. Hochbaum and P. Yang, Chem. Rev. **110**, 527 (2009).
[4] R. Yan, D. Gargas, and P. Yang, Nat. Photonics **3**, 569 (2009).
[5] P. Yang, R. Yan, and M. Fardy, Nano Lett. **10**, 1529 (2010).
[6] W. Tang and D. Cameron, Thin Solid Films **280**, 221 (1996).
[7] X. Fang *et al.*, Adv. Mater. **21**, 2034 (2009).
[8] X. Fang, L. Wu, and L. Hu, Adv. Mater. **23**, 585 (2011).
[9] X. Fang, T. Zhai, U. K. Gautam, L. Li, L. Wu, Y. Bando, and D. Golberg, Prog. Mater. Sci. **56**, 175 (2011).
[10] C. Lan, K. Hong, W. Wang, and G. Wang, Solid State Commun. **125**, 455 (2003).
[11] X. S. Fang, C. H. Ye, X. S. Peng, Y. H. Wang, Y. C. Wu, and L. D. Zhang, J. Cryst. Growth **263**, 263 (2004).
[12] X. S. Fang, C. H. Ye, L. D. Zhang, Y. H. Wang, and Y. C. Wu, Adv. Funct. Mater. **15**, 63 (2005).
[13] Z. Wang, L. L. Daemen, Y. Zhao, C. Zha, R. T. Downs, X. Wang, Z. L. Wang, and R. J. Hemley, Nat. Mater. **4**, 922 (2005).
[14] C. Cheng, G. Xu, H. Zhang, J. Cao, P. Jiao, and X. Wang, Mater. Lett. **60**, 3561 (2006).
[15] X. J. Xu, G. T. Fei, W. H. Yu, X. W. Wang, L. Chen, and L. D. Zhang, Nanotechnology **17**, 426 (2006).
[16] X. Fang, Y. Bando, C. Ye, G. Shen, and D. Golberg, J. Phys. Chem. C **111**, 8469 (2007).
[17] C. Y. Yeh, Z. Lu, S. Froyen, and A. Zunger, Phys. Rev. B **46**, 10086 (1992).
[18] Y. Li, J. Tang, H. Wang, J. Zapien, Y. Shan, and S. Lee, Appl. Phys. Lett. **90**, 093127 (2007).
[19] Y. Jiang, W. J. Zhang, J. S. Jie, X. M. Meng, J. A. Zapien, and S. T. Lee, Adv. Mater. **18**, 1527 (2006).
[20] H. S. Chung, Y. Jung, T. J. Zimmerman, S. H. Lee, J. W. Kim, S. H. Lee, S. C. Kim, K. H. Oh, and R. Agarwal, Nano Lett. **8**, 1328 (2008).
[21] M. S. Gudiksen, L. J. Lauhon, J. Wang, D. C. Smith, and C. M. Lieber, Nature **415**, 617 (2002).
[22] M. W. Larsson, J. B. Wagner, M. Wallin, P. Håkansson, L. E. Fröberg, L. Samuelson, and L. R. Wallenberg, Nanotechnology **18**, 015504 (2007).
[23] M. Paladugu, J. Zou, Y. N. Guo, G. J. Auchterlonie, H. J. Joyce, Q. Gao, H. Hoe Tan, C. Jagadish, and Y. Kim, Small **3**, 1873 (2007).
[24] K. A. Dick, C. Thelander, L. Samuelson, and P. Caroff, Nano Lett. **10**, 3494 (2010).
[25] M. Heiss *et al.*, Phys. Rev. B **83**, 045303 (2011).
[26] D. Spirkoska *et al.*, Phys. Rev. B **80**, 245325 (2009).
[27] P. Caroff, K. A. Dick, J. Johansson, M. Messing, K. Deppert, and L. Samuelson, Nat. Nanotechnol. **4**, 50 (2008).
[28] J. Johansson, K. Dick, P. Caroff, M. Messing, J. Bolinsson, K. Deppert, and L. Samuelson, J. Phys. Chem. C **114**, 3837 (2010).
[29] H. J. Joyce, J. Wong-Leung, Q. Gao, H. H. Tan, and C. Jagadish, Nano Lett. **10**, 908 (2010).
[30] T. Yamashita, T. Akiyama, K. Nakamura, and T. Ito, Physica E **42**, 2727 (2010).
[31] K. Wang *et al.*, Appl. Phys. Lett. **96**, 123105 (2010).
[32] M. Y. Lu, J. Song, M. P. Lu, C. Y. Lee, L. J. Chen, and Z. L. Wang, ACS Nano **3**, 357 (2009).
[33] J. Yan, X. Fang, L. Zhang, Y. Bando, U. K. Gautam, B. Dierre, T. Sekiguchi, and D. Golberg, Nano Lett. **8**, 2794 (2008).
[34] L. Hu, J. Yan, M. Liao, H. Xiang, X. Gong, L. Zhang, and X. Fang, Adv. Mater. **24**, 2305 (2012).
[35] C. Ma, D. Moore, J. Li, and Z. L. Wang, Adv. Mater. **15**, 228 (2003).
[36] J. Jie, W. Zhang, Y. Jiang, X. Meng, J. Zapien, M. Shao, and S. Lee, Nanotechnology **17**, 2913 (2006).
[37] H. Zhang, J. Zhang, T. Xu, M. He, and J. Li, RSC Adv. **3**, 3535 (2013).
[38] N. Akopian, G. Patriarche, L. Liu, J.-C. Harmand, and V. Zwiller, Nano Lett. **10**, 1198 (2010).
[39] A. Kulkarni, K. Sarasamak, J. Wang, F. Ke, S. Limpijumnong, and M. Zhou, Mech. Res. Commun. **35**, 73 (2008).
[40] K. Jung, M. Cho, and M. Zhou, J. Appl. Phys. **112**, 083522 (2012).
[41] K.-H. Lin and A. Strachan, Phys. Rev. B **87**, 115302 (2013).
[42] V. Samvedi and V. Tomar, J. Phys. D: Appl. Phys. **43**, 135401 (2010).
[43] K. Termentzidis, T. Barreteau, Y. Ni, S. Merabia, X. Zianni, Y. Chalopin, P. Chantrenne, and S. Volz, Phys. Rev. B **87**, 125410 (2013).
[44] M. Bachmann, M. Czerner, S. Edalati-Boostan, and C. Heiliger, Eur. Phys. J. B **85**, 146 (2012).
[45] M. S. Dresselhaus, G. Chen, M. Y. Tang, R. Yang, H. Lee, D. Wang, Z. Ren, J. P. Fleurial, and P. Gogna, Adv. Mater. **19**, 1043 (2007).
[46] Y.-M. Lin and M. Dresselhaus, Phys. Rev. B **68**, 075304 (2003).
[47] D. G. Cahill, W. K. Ford, K. E. Goodson, G. D. Mahan, A. Majumdar, H. J. Maris, R. Merlin, and S. R. Phillpot, J. Appl. Phys. **93**, 793 (2003).
[48] C. Panse, D. Kriegner, and F. Bechstedt, Phys. Rev. B **84**, 075217 (2011).
[49] D. Kriegner *et al.*, Nano Lett. **11**, 1483 (2011).
[50] Y. Chalopin, K. Esfarjani, A. Henry, S. Volz, and G. Chen, Phys. Rev. B **85**, 195302 (2012).
[51] E. Landry and A. McGaughey, Phys. Rev. B **80**, 165304 (2009).
[52] S. Plimpton, J. Comput. Phys. **117**, 1 (1995).
[53] W. G. Hoover, Phys. Rev. A **31**, 1695 (1985).
[54] K. Wright and R. A. Jackson, J. Mater. Chem. **5**, 2037 (1995).
[55] D. Wolf, P. Keblinski, S. Phillpot, and J. Eggebrecht, J. Chem. Phys. **110**, 8254 (1999).
[56] J. Wang, P. Xiao, M. Zhou, Z. Wang, and F. Ke, J. Appl. Phys. **107**, 023512 (2010).
[57] J. Wang, A. Kulkarni, F. Ke, Y. Bai, and M. Zhou, Comput. Methods Appl. Mech. Eng. **197**, 3182 (2008).
[58] S. Koh and H. Lee, Nanotechnology **17**, 3451 (2006).
[59] S. Koh, H. Lee, C. Lu, and Q. Cheng, Phys. Rev. B **72**, 085414 (2005).
[60] H. Wu, Eur. J. Mech. A **25**, 370 (2006).
[61] S. G. Volz and G. Chen, Phys. Rev. B **61**, 2651 (2000).
[62] I. Feranchuk, A. Minkevich, and A. Ulyanenkov, Eur. Phys. J. Appl. Phys. **19**, 95 (2002).
[63] C.-E. Hu, Z.-Y. Zeng, Y. Cheng, X.-R. Chen, and L.-C. Cai, Chin. Phys. B **17**, 3867 (2008).
[64] F. Müller-Plathe, J. Chem. Phys. **106**, 6082 (1997).
[65] A. France-Lanord, S. Merabia, T. Albaret, D. Lacroix, and K. Termentzidis, J. Phys.: Condens. Matter **26**, 355801 (2014).
[66] A. France-Lanord, E. Blandre, T. Albaret, S. Merabia, D. Lacroix, and K. Termentzidis, J. Phys.: Condens. Matter **26**, 055011 (2014).
[67] K. Termentzidis, A. France-Lanord, E. Blandre, T. Albaret, S. Merabia, V. Jean, and D. Lacroix, MRS Proc. **1543**, 71 (2013).
[68] Y. Zhou, B. Anglin, and A. Strachan, J. Chem. Phys. **127**, 184702 (2007).
[69] I. Ponomareva, D. Srivastava, and M. Menon, Nano Lett. **7**, 1155 (2007).
[70] M. Zhou, Proc. R. Soc. London, Ser. A **459**, 2347 (2003).
[71] C. Tiwary, P. Kumbhakar, A. Mondal, and A. Mitra, Phys. Status Solidi A **207**, 1874 (2010).
[72] B. J. Morgan, Phys. Rev. B **78**, 024110 (2008).
[73] B. J. Morgan, Phys. Rev. B **82**, 153408 (2010).
[74] R. Dingreville, A. J. Kulkarni, M. Zhou, and J. Qu, Modell. Simul. Mater. Sci. Eng. **16**, 025002 (2008).
[75] B. Fu, N. Chen, Y. Xie, X. Ye, and X. Gu, Phys. Lett. A **377**, 2681 (2013).
[76] S. Bhowmick and V. B. Shenoy, J. Chem. Phys. **125**, 164513 (2006).
[77] G. A. Slack, Phys. Rev. B **6**, 3791 (1972).
[78] D. Spitzer, J. Phys. Chem. Solids **31**, 19 (1970).
[79] C. Guthy, C.-Y. Nam, and J. E. Fischer, J. Appl. Phys. **103**, 064319 (2008).
[80] P. J. Hegedus and A. R. Abramson, Int. J. Heat Mass Transfer **49**, 4921 (2006).
[81] E. T. Swartz and R. O. Pohl, Rev. Mod. Phys. **61**, 605 (1989).
[82] V. Samvedi and V. Tomar, Nanotechnology **20**, 365701 (2009).
[83] Y. Chen, D. Li, J. Yang, Y. Wu, J. R. Lukes, and A. Majumdar, Physica B **349**, 270 (2004).
[84] A. S. Henry and G. Chen, J. Comput. Theor. Nanosci. **5**, 141 (2008).
[85] C. F. Cline, H. L. Dunegan, and G. W. Henderson, J. Appl. Phys. **38**, 1944 (1967).
[86] H. Chen, D. Shi, J. Qi, and B. Wang, Physica E **42**, 32 (2009).
[87] K. Wright and J. D. Gale, Phys. Rev. B **70**, 035211 (2004).